NRC Publications Archive
Archives des publications du CNRC

Time- and frequency-resolved coherent anti-Stokes Raman scattering spectroscopy with sub-25 fs laser pulses

Lausten, Rune; Smirnova, Olga; Sussman, Benjamin J.; Gräfe, Stefanie; Mouritzen, Anders S.; Stolow, Albert

NRC Publications Archive Record / Notice des Archives des publications du CNRC :
https://nrc-publications.canada.ca/eng/view/object/?id=0fe78fea-ca86-40e8-b36e-af39312a8615
https://publications-cnrc.canada.ca/fra/voir/objet/?id=0fe78fea-ca86-40e8-b36e-af39312a8615

Questions? Contact the NRC Publications Archive team at
PublicationsArchive-ArchivesPublications@nrc-cnrc.gc.ca. If you wish to email the authors directly, please see the first page of the publication for their contact information.

Vous avez des questions? Nous pouvons vous aider. Pour communiquer directement avec un auteur, consultez la première page de la revue dans laquelle son article a été publié afin de trouver ses coordonnées. Si vous n'arrivez pas à les repérer, communiquez avec nous à PublicationsArchive-ArchivesPublications@nrc-cnrc.gc.ca.

National Research Council Canada   Conseil national de recherches Canada

Canada

Time- and frequency-resolved coherent anti-Stokes Raman scattering spectroscopy with sub-25 fs laser pulses

Rune Lausten,[1,2,a)] Olga Smirnova,[2] Benjamin J. Sussman,[1] Stefanie Gräfe,[2] Anders S. Mouritzen,[3] and Albert Stolow[1,2]

[1]*Department of Physics, Queen's University, Kingston, Ontario K7L 3N6, Canada*
[2]*Steacie Institute for Molecular Sciences, National Research Council of Canada, Ottawa, Ontario K1A 0R6, Canada*
[3]*Department of Physics and Astronomy, University of Aarhus, DK-8000 Århus C, Denmark*

In general, many different diagrams can contribute to the signal measured in broadband four-wave mixing experiments. Care must therefore be taken when designing an experiment to be sensitive to only the desired diagram by taking advantage of phase matching, pulse timing, sequence, and the wavelengths employed. We use sub-25 fs pulses to create and monitor vibrational wavepackets in gaseous iodine, bromine, and iodine bromide through time- and frequency-resolved femtosecond coherent anti-Stokes Raman scattering (CARS) spectroscopy. We experimentally illustrate this using iodine, where the broad bandwidths of our pulses, and Boltzmann population in the lower three vibrational levels conspire to make a single diagram dominant in one spectral region of the signal spectrum. In another spectral region, however, the signal is the sum of two almost equally contributing diagrams, making it difficult to directly extract information about the molecular dynamics. We derive simple analytical expressions for the time- and frequency-resolved CARS signal to study the interplay of different diagrams. Expressions are given for all five diagrams which can contribute to the CARS signal in our case. © *2008 American Institute of Physics.*
[DOI: 10.1063/1.2932101]

I. INTRODUCTION

There is considerable effort devoted to the generation of increasingly shorter pulses of visible light. The development of ultrashort pulse Ti:sapphire oscillators has led to near-infrared (NIR) pulses shorter than 7 fs at 800 nm (Refs. 1 and 2) and tunable visible pulses as short as 29 fs from 400 nm synchronously pumped optical parametric oscillators.[3] For amplified laser pulses, the development of the noncollinear optical parametric amplifier[4] (NOPA) has produced pulses in the visible and NIR region as short as 5 fs.[5] These, in combination with broadband phase matching schemes for second harmonic generation, have resulted in UV pulses below 10 fs in duration.[6] One of the most important applications of this technology is to problems in condensed phase molecular dynamics where ultrafast electronic dephasing times often obscure the spectroscopic and dynamical information being sought. In order to address these issues, various nonlinear optical (NLO) spectroscopies have been developed[7] which help disentangle the various contributions of the material response to applied optical laser fields. Due to the inversion symmetry of molecules in bulk noncrystalline media, the lowest order NLO response of general utility is at third order, of which coherent anti-Stokes Raman scattering (CARS) is a well known example. When combined with ultrashort laser pulses, CARS can reveal detailed dynamics within excited molecules in both gas[8,9] and condensed phases. The CARS process involves the interac-

tion of three laser fields, generating a third order polarization whose associated emitted field is measured in a phase-matched direction. As discussed by Faeder *et al.*,[10] the expression for the third order polarization includes all possible time orderings of the three interactions. The spectroscopic pathways producing the third order polarization may be depicted using double-sided Feynman diagrams, as shown, for example, in Fig. 3 of Ref. 10.

In this paper we consider the case where a pump and Stokes pulse always overlap and only five of the eight different diagrams given in Ref. 10 can contribute to the femtosecond time-resolved CARS signal, depending on the delays. Defining the pump/Stokes pulse pair overlap as $t=0$, the situation where the delayed pump pulse arrives before (after) $t=0$ thus corresponds to negative (positive) delays. These diagrams and their labels are reproduced from Ref. 11 in Fig. 1.

For "cold" molecules we need only consider diagram A for $\Delta t < 0$ and diagram C for $\Delta t > 0$, since diagrams B, D, and E all require excited vibrational states to be populated, e.g., via the Boltzmann distribution at a finite temperature.

For the case of "hot" molecules, it is sometimes possible to suppress contributions from the unwanted diagrams. More generally, however, all contributions must be considered and the detected signal is the coherent sum of the fields due to each diagram. These fields, for the case of homodyne detection, are then squared on the detector, leading to various cross terms and interferences.

In the present paper we focus on the femtosecond time-resolved CARS signal for negative time delays. The selec-

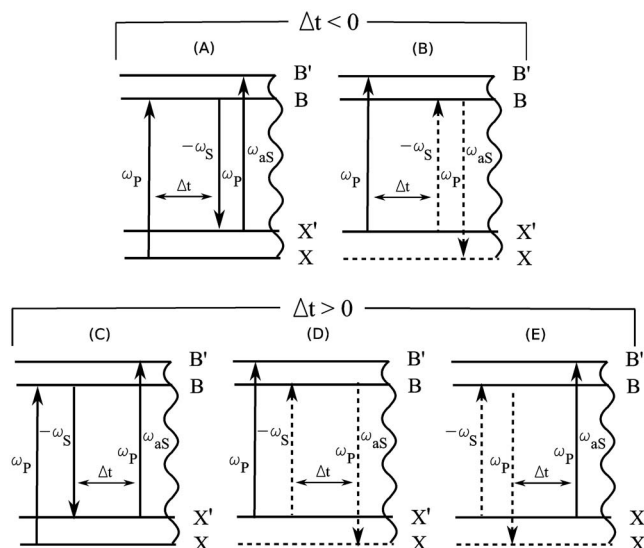a)Electronic mail: rune.lausten@nrc.ca.

FIG. 1. Energy level diagrams, illustrating the vibrationally resonant interactions contributing to the femtosecond time-resolved CARS signal for negative and positive delays between the pump/Stokes pulse pair at $t = 0$ and the delayed pump pulse. The interactions with the pump (p) pulse and the pump (p)/Stokes (S) pulse pair are sketched. When very short pulses are used (e.g., sub-25 fs), the scattered signals arising from these interactions may be spectroscopically overlapping, leading to polarization beats which dramatically affect the form of the pump-probe signals. In complex samples or environments, it may not be possible to ensure that only one interaction dominates, especially when ultrashort pulses are applied (Ref. 7). These diagrams are reproduced from Ref. 11. The corresponding Feynman diagrams can be seen in Ref. 10.

tion mechanisms which apply to hot molecules have been discussed by Faeder *et al.*:[10] There are two complementary factors which can lead to suppression of diagram B. First, if the detuning between the Stokes and pump pulses, ($E_v - E_0 = \omega_p - \omega_S$), is large compared with the vibrational level spacing and $k_B T$, diagram B will be suppressed since there will be no population in the vibrationally excited state, E_v, from which the Stokes photon can be absorbed. Second, the pump wavelength is usually chosen close to the maximum of the electronic absorption band, and the Stokes shift chosen large enough for the Stokes pulse to be away from this resonance. Consequently, even if the vibrational levels E_v required for the first condition are populated, the absorption cross section for the Stokes pulse can be small, favoring energy level diagram A over diagram B.

Important to the present paper is the fact that these criteria become difficult to fulfill when ultrashort pulses are used: the inherently very broad bandwidths of sub-25 fs pulses can lead to Stokes shifts that are still within spectral overlap of the pulses involved. If neither of the above criteria are met, then both diagram contribute to the third order signal propagating in the phase-matched direction.

Ultrashort pulse CARS spectroscopy of complex samples requires more careful consideration of the various interactions in order to properly describe the observed signals. Unfortunately, the complexity of some systems and/or environments may make assessment of these criteria quite challenging. Our goals here are to (i) clearly illustrate the case for ultrashort pulse CARS spectroscopy when both processes shown in Fig. 1 are involved and (ii) discuss how one

can treat the interfering contributions to the measured signal. In the following, we use both experimental results from sub-25 fs CARS spectroscopy and a simple analytical model describing the CARS process. We have chosen the well known gas phase system molecular iodine I_2, which was heated to 360 K in order to increase its vapor pressure. At these temperatures, three to four vibrational levels are populated within the ground electronic state, and the contribution from each of these states has to be considered separately.

Iodine I_2 was one of the first systems to be systematically studied using femtosecond pump-probe spectroscopy in the gas phase.[12,13] Iodine has long served as a model system in the development of new femtosecond techniques such as time-resolved photoelectron spectroscopy,[14] time-resolved Coulomb explosion,[15] and femtosecond coherent nonlinear spectroscopies.[8,16] The dynamics of I_2 was also used to study the femtosecond spectroscopy of complex environments such as rare gas collisional systems,[17] cryogenic matrices,[18] and zeolites.[19] Relevant to the present effort, detailed studies by Knopp *et al.*[20] demonstrated the virtues of using I_2 as a model system for studies in femtosecond coherent nonlinear spectroscopy and control.

In the following, we present our combined experimental-theoretical studies of femtosecond time- and frequency-resolved CARS spectroscopy of gas phase iodine (I_2),[21] bromine (Br_2), and iodine bromide (IBr). In order to address the issues discussed above, we used ≤ 25 fs duration pulses and heated samples ensuring a broad Boltzmann distribution of rotational and vibrational states. We spectrally dispersed the signals scattered into the phase-matched direction, revealing both details of the wavepacket dynamics and the interfering contributions from the involved diagrams. Under isolated conditions, the induced coherence can persist for extremely long times, leading to the observation of wavepacket revivals[22] and fractional revivals.[23–27] The revivals and fractional revivals of vibrational wavepackets in diatomic molecules were studied experimentally for a number of systems, including the molecules of interest here, iodine,[12–14,28] bromine,[29,30] and iodine bromide.[31,32]

Finally, as described in the Appendix, we outline a simple analytical model for calculating the third order polarizations based on the pole approximation, permitting a clear view of the contributions from the different diagrams. Our results illustrate how time- and frequency-resolved four-wave mixing with ultrashort pulses can lead to the observation of regular or apparently irregular wavepacket dynamics, depending on which observation window is chosen for the spectrally resolved scattered signal. In ultrashort pulse coherent nonlinear spectroscopies of complex systems/environments, we expect that unambiguous extraction of the underlying molecular dynamics from these observables will generally require considerations of the type discussed here.

II. TIME-RESOLVED FREQUENCY INTEGRATED CARS SIGNAL

In a well designed third order experiment, one would prefer the polarization to be dominated by a single diagram. This arguably yields the most transparent view of the under-

lying molecular dynamics which modulates the observed signals. Central to this paper, however, is the fact that this "single diagram" picture will fail for as simple a sample as gas phase I_2 at 360 K, probed by sub-25 fs laser pulses. In order to understand the consequences, we begin by considering the contribution to the CARS signal at $t<0$ from the single diagram labeled A in Fig. 1. For a homodyne detection scheme, the transient CARS signal is calculated by time integrating the third order polarization $P^{(3)}$ as

$$S(\Delta t) = \int_{-\infty}^{\infty} dt |P^{(3)}(t, \Delta t)|^2. \tag{1}$$

Here t is the time and Δt denotes the positive temporal separation between the single pump pulse and the Stokes/pump pulse pair. The polarization is given as

$$P^{(3)}(t, \Delta t) = \sum_{n=0}^{3} \langle \psi^{(3-n)}(t, \Delta t)|\hat{\mu}|\psi^{(n)}(t, \Delta t)\rangle, \tag{2}$$

where $\hat{\mu}$ is the dipole operator [after averaging over electronic degrees of freedom, $\hat{\mu}(R)$ connecting the ground and excited electronic state is replaced with a constant in the Condon approximation]. The brackets denote integration over the bondlength R and the wave functions determined within j'th order perturbation theory are denoted as $\psi^{(j)}$.

The CARS signal, originating from the matrix element a_{03}:

$$a_{03}(t, \Delta t) = \langle \psi^{(0)}(R, t)|\hat{\mu}|\psi^{(3)}(R, t, \Delta t)\rangle, \tag{3}$$

oscillates as a function of time delay Δt, and contains beat frequencies corresponding to energy level spacings in the electronically excited state. Therefore, the time-resolved CARS signal is a direct reflection of the vibrational wavepacket motion in the excited state, the dynamics of which is well known.[29,30] An example of an excited state CARS transient calculated by numerical wavepacket propagation, using techniques similar to those used by Meyer et al.[33] (with parameters pertaining to our experiment), can be seen in Fig. 2. In these calculations we include only the vibrational degree of freedom, since the role of the many rotational levels has been investigated previously.[34] The fast Fourier transform (FFT) of this transient is shown in Fig. 3.

The fundamental peak in the FFT shows coherences between nearest-neighbor vibrational levels and is centered on the average vibrational frequency of the wavepacket (ω_ν). When resolved in the FFT,[29,30] each peak corresponds to the vibrational energy level splitting between ν and its nearest-neighbor $\nu+1$. The peaks at this fundamental frequency are separated by the vibrational anharmonicity term $\omega_e \chi_e$. In the present case, however, we do not resolve the individual peaks in the fundamental frequency region due to the calculation being truncated before the full revival. At the second harmonic frequency, another peak centered at ($2\omega_\nu$) can be seen, corresponding to coherences between next nearest neighbors, ν and $\nu+2$. The splitting between peaks in this case[29,30] is thus $2\omega_e \chi_e$. The still higher order coherences are to be understood in an analogous manner. These results illustrate how, when a single CARS diagram is involved, the measured signal transparently reflects details of the excited
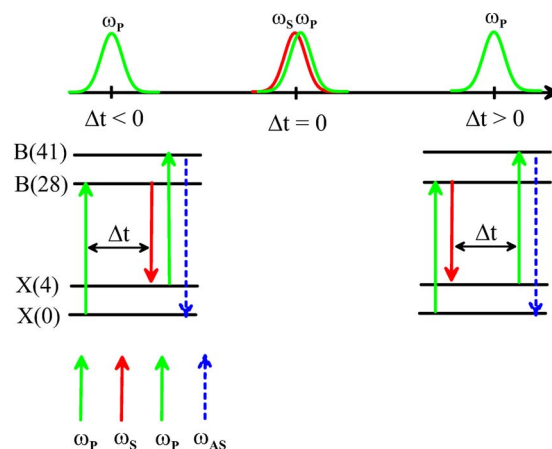

FIG. 2. (Color online) Pulse and level scheme for the time-resolved CARS experiments on "cold" molecules, illustrating how either excited state or ground state dynamics can be studied, depending on the delay. For $\Delta t<0$ via diagram A, for $\Delta t>0$ through diagram C of Fig. 1. The third order process involves a pump pulse (ω_p) delayed with respect to the Stokes/pump pulse pair (ω_S/ω_p). These three fields generate a third order polarizability in the molecules, leading to emission of the CARS signal at the anti-Stokes frequency (ω_{AS}). All polarizations are parallel, as shown in the lower diagram.

state vibrational wavepacket dynamics. As we discuss in the following, when the single diagram picture fails (our case), the observed signals do not so transparently reflect the molecular dynamics and both time-resolved and frequency-resolved measurements are required to disentangle the contributions of different diagrams.

III. EXPERIMENTAL

For our experiments, we constructed a dispersion-free, polarization maintaining time- and frequency-resolved CARS spectrometer. Several groups have previously shown how time resolving the electronically resonant CARS pro-
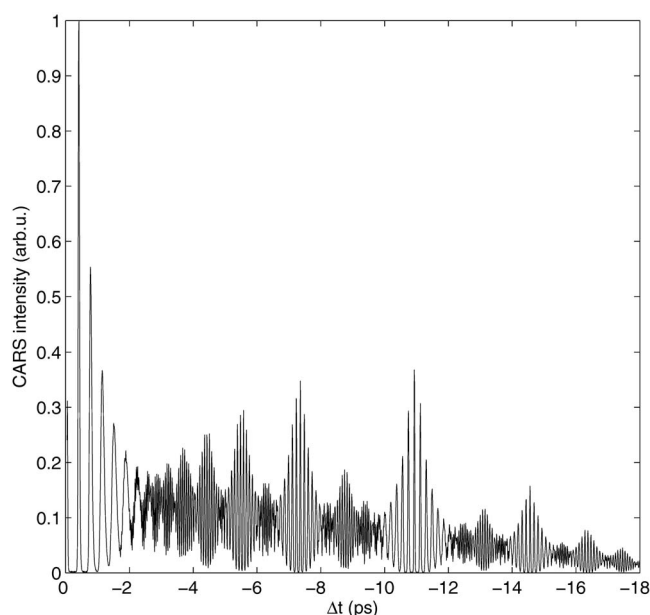

FIG. 3. Calculated CARS signal for wavepacket dynamics in the I_2 B-state, using the method described in Sec. II. The parameters were chosen so as to correspond to our experimental conditions.
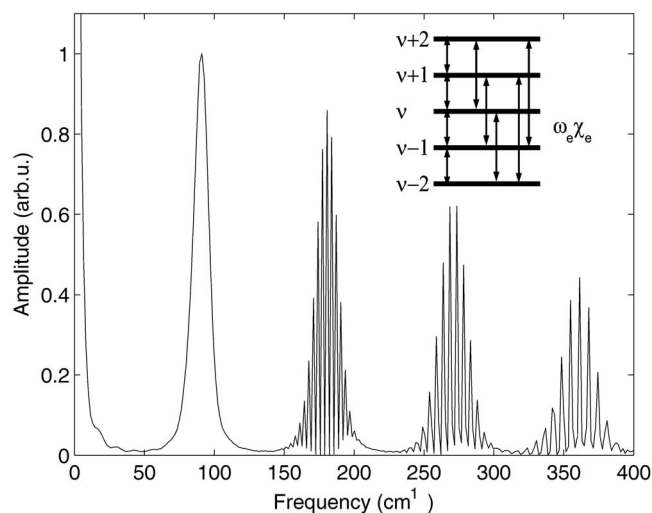
FIG. 4. The Fourier transform of the CARS signal from Fig. 3. The inset shows how coherences between different vibrational levels of the wavepacket give rise to the peaks in the Fourier transform. Details are discussed in the text.

cess can be used to study both ground and excited state dynamics in I_2 by detection at a particular wavelength,[16,35] or by dispersed broadband detection.[8,36] We therefore summarize only briefly. Defining the overlap of pump/Stokes pulses to be $t=0$, we introduce a delay Δt of the second pump interaction with respect to this. If we now tune the wavelengths of the pump/Stokes pulses responsible for the CARS process into the $B(^3\Pi_{0u}^+) \leftarrow X(^1\Sigma_{0g}^+)$ electronic resonance, the CARS signal will probe either the dynamics of the ground or excited state depending on the delay between the single pump pulse, and the pump/Stokes pulse pair. For negative delays, the single pump pulse arrives first, creating a vibrational wavepacket in the excited state, which can then later be probed by the Stokes/pump pulse pair. For positive delays, the pump/Stokes pulse pair creates a vibrational wavepacket in the ground electronic state, the dynamics of which can be followed by scanning the delay of the last pump pulse completing the CARS process (see Fig. 4). Specifically using parameters relevant to the experiment, we start from the ground state, at thermal equilibrium at 360 K, with a 25 fs pump pulse centered at 540 nm. This creates a vibrational wavepacket in the B-state of iodine centered at $v'=28$ and spanning nine to ten vibrational levels. The wavepacket undergoes field-free evolution and is subsequently probed through interaction with the 25 fs Stokes pulse centered at 565 nm and the second pump pulse, thus completing the CARS sequence. By spectrally dispersing the anti-Stokes signal, we discern the time- and frequency-resolved wavepacket
dynamics.

A block diagram of the experimental arrangement is given in Fig. 5. The samples iodine, bromine, or (purified) iodine bromide were introduced into a heatable closed quartz cell with thin (1 mm) fused silica windows.

The three ultrashort optical pulses required for the CARS experiment are derived from a Ti:sapphire oscillator and 1 kHz regenerative amplifier system, as shown in Fig. 5. Approximately 500 μJ/pulse (80 fs at 800 nm) of the ampli-
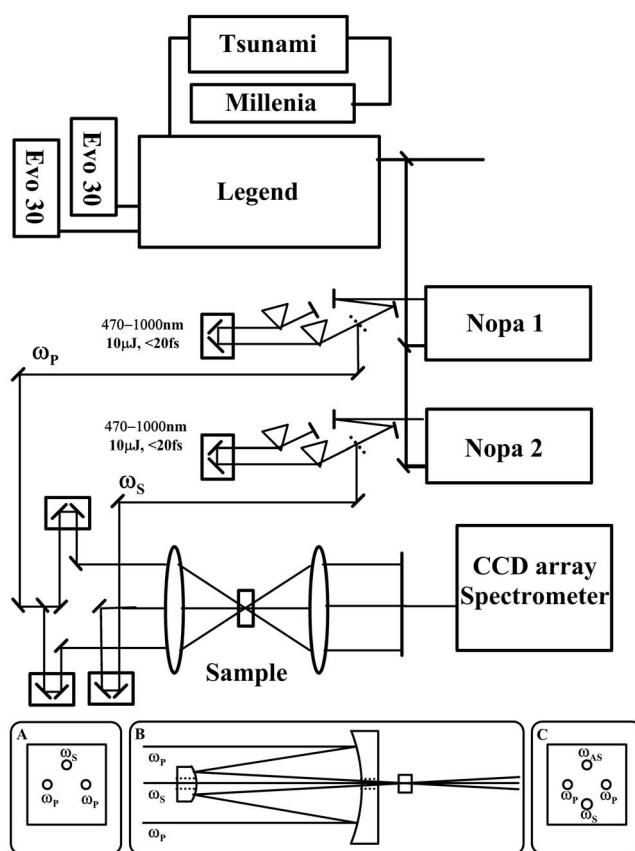

FIG. 5. Dispersion-free, polarization maintaining time- and frequency-resolved CARS spectrometer. A regenerative Ti:sapphire amplifier produces 80 fs pulses pumping two NOPAs, each yielding tunable sub-20 fs optical pulses. Three optical delay lines control their relative timing. The beams are arranged in the folded-BOXCARS configuration and focused using an all-reflective Cassegrain setup, which is dispersion-free and polarization maintaining. Details of this setup are shown in insets A–C. The CARS process generates a third order response at the common focus and leads to emission of anti-Stokes radiation in the phase-matched direction. The CARS signal is dispersed in an imaging spectrometer, where its full spectrum can be collected at each time delay.

fied light is used to pump two NOPAs, resulting in widely tunable sub-20 fs pulses with pulse energies of $\sim$10 μJ. One of the NOPA pulses, acting as the pump in the CARS process, was split by a 1 mm thick inconel coated quartz beamsplitter. The three CARS pulses were delayed appropriately with computer controlled stages, and overlapped in the noncollinear folded-BOXCARS beam geometry. This ensures that the CARS signal propagates in a direction different from the three input beams and can therefore be collected background-free. In addition, it also rules out contributions from other third order processes which do not phase match in this same direction.

Due to the problems with the dispersion management of sub-20 fs pulses, we employed a Cassegrain-based geometry for focusing (inset in Fig. 5). This has the advantage, due to its all-reflective design, of being both achromatic and dispersion-free. In addition, due to the small angles ($\sim$1.8°) of incidence, this geometry minimizes any polarization rotation due to reflection from metal surfaces and therefore is polarization maintaining. Finally, we note that this geometry is ideal for bringing a fourth beam along the centerline of the
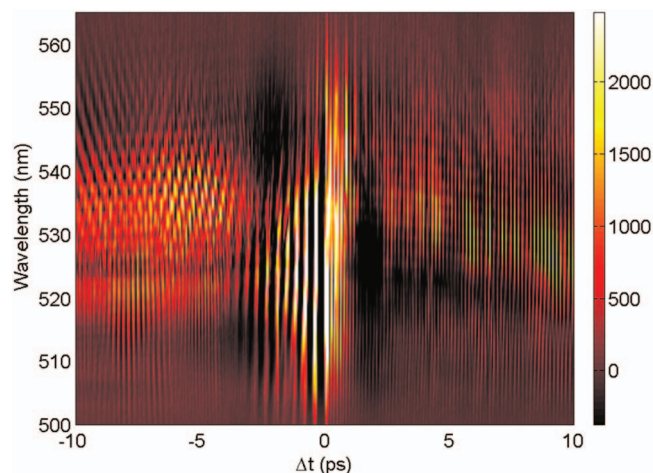
FIG. 6. (Color) Time- and frequency-resolved femtosecond CARS spectrum of iodine. The ordinate is the time delay between single pump and the Stokes/pump pulse pair. This 2D data set contains a wealth of information about both excited and ground state dynamics, most clearly illustrated by taking cuts at particular wavelengths λ_{AS}. Aside from canonical wavepacket dynamics, the data also reveal interesting beating patterns related to the interference between different contributions to the third order polarization. For a detailed discussion, see the text.
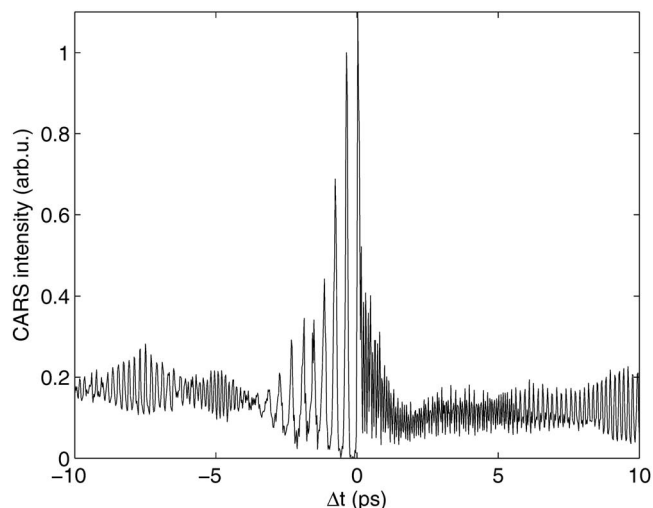

FIG. 7. A cut through the CARS data at $\lambda_{AS}=520$ nm from Fig. 6. For negative time delays, excited state dynamics is observed, ground state dynamics for positive delays. Based on the center wavelengths of the pump and Stokes pulses, this cut corresponds to where the CARS signal is expected to be strongest.

Cassegrain, allowing for pump-FWM experiments, where the three-pulse FWM scheme can be used to study multiple timescale dynamics induced by a fourth pump pulse.[37]

The CARS signal was spatially separated from the Stokes and pump beams by an iris, collimated with a lens and propagated a long path length ($\sim$20 m) in order to remove residual scattered light background. It was then spectrally dispersed in an $f=300$ mm imaging spectrometer (Acton SP300i) and detected by a 1024×252 pixel cooled charge coupled device (CCD) array detector. An electronic shutter built into the spectrometer controlled the average light exposure. Typically 500–1000 pulses were averaged on the CCD chip per time delay step. The quartz sample cell was heated, for iodine, to a temperature of 360 K, corresponding to a vapor pressure of 35 Torr. For bromine and iodine bromide, the sample cell was at room temperature (due to their higher vapor pressures).

IV. RESULTS AND DISCUSSION

In Fig. 6 we present the time- and frequency-resolved CARS spectrum for iodine. As discussed in Sec. III, the $\sim$25 fs pump and Stokes pulses were chosen to be electronically resonant with the $B \leftarrow X$ transition. The time delay was scanned ± 10 ps in steps of 25 fs. It can be seen that, due to the ultrashort input pulses, the spectrum of the scattered third order signal is very broad—about 50 nm wide. For the input wavelengths used in this experiment, we would expect to find the anti-Stokes signal centered at $\omega_{AS}=2\omega_P-\omega_S$ $=19\,181$ cm^{-1} (519 nm). The data show clear evidence of two regions, at negative and positive time delays, exhibiting different behavior.

As an illustrative example, we take a cut along the line at $\lambda_{AS}=520$ nm, shown in Fig. 7, where the center of the anti-Stokes spectrum is expected. The well known B-state wavepacket dynamics is seen at negative time delays whereas

X-state dynamics is seen at positive time delays. In Fig. 8 we show the FFT power spectra of the data from Fig. 7. Again, these power spectra show that the $\Delta t < 0$ and $\Delta t > 0$ regions correspond to the observation of vibrational wavepacket dynamics in either excited B-state or ground state X-state, respectively.

We concentrate herein on excited state wavepacket dynamics, corresponding to negative time delays where the pump pulse creates a wavepacket in the excited B-state which is then probed as a function of the delay Δt of the Stokes/pump pulse pair. We take four illustrative cuts of the two-dimensional (2D) data in Fig. 6 at $\lambda_{AS}=515$, 520, 525, and 545 nm. These are shown in Figs. 9(a)–9(d), respectively. The (A)–(C) plots show quite similar behavior: a strong oscillation with an average period of 400 fs from 0 to 4 ps, which revives at 17 ps and again 34 ps (not shown), corresponding to vibrational wavepacket dynamics in the excited B-state. Due to the anharmonicity of the potential, the wavepacket spreads (or dephases) but undergoes a series of rephasings and partial rephasings, leading to revival and fractional revival structures.[23,29] The initially prepared wavepacket is recreated at the full revival at 34 ps (not shown). The initial wavepacket can also reform on the outer turning point of the potential, called a half revival,[23,29] as observed at 17 ps. An interesting behavior is observed in the intermediate region, where the wavepacket goes through various fractional revivals. For example, at the quarter revival, the wavepacket is split into two equal parts exactly out of phase, leading to the doubling of the modulation frequency as clearly seen in the data. At the one-sixth revival, the wavepacket is split into three equal parts, leading to a tripling of the modulation frequency, and so on.[23,29] Note that the magnitude of the revivals is significantly lower than that of the initial wavepacket oscillation (first 4 ps) due to the decay of the rotational anisotropy that was created by the first pump pulse. If desired, this can be avoided by using magic angle detection, as previously described.[9]
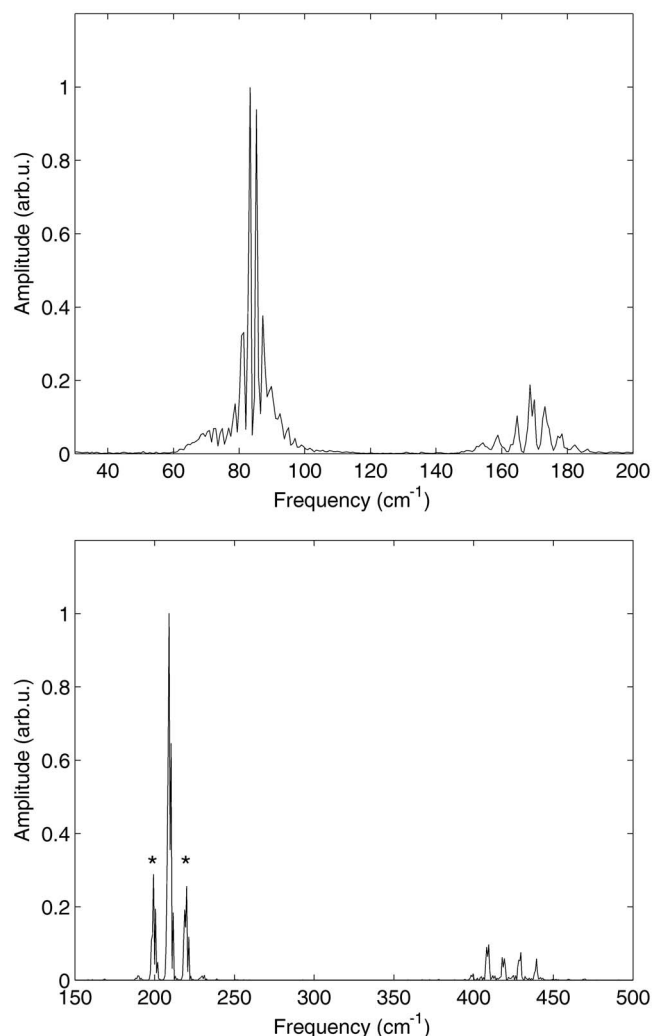
FIG. 8. Fourier transform power spectra of the iodine transient at λ_{AS} =520 nm, from Fig. 7, for negative (top) and positive (bottom) time delays. The line spacings in the power spectra correspond, as expected, to level spacings in the excited *B*-state and the ground *X*-state, respectively. The peaks marked * in the lower panel are due to polarization beats, as discussed in the text.

FIG. 9. Four cuts of the time- and frequency-resolved femtosecond iodine CARS data from Fig. 6, showing transients at λ_{AS}=515, 520, 525, and 545 nm, respectively. In panel (B), canonical wavepacket dynamics is seen and the fundamental vibrational period of 400 fs is indicated, along with the locations of the various fractional revivals. While (A)–(C) show similar behavior, panel (D) appears strikingly different and does not simply reflect the wavepacket dynamics. For a discussion, see the text.

As shown in Fig. 10, Fourier transform power spectra of the data in Figs. 9(a)–9(c) confirm that the oscillations in the transients result from a coherent superposition of vibrational eigenstates with energy spacings centered around 83 cm^{-1}. This corresponds to the spacing between two neighboring vibrational eigenstates in the anharmonic region of the *B*-state in iodine at v'=28, the levels accessed by the pump pulse at 540 nm. Comparing the FFT power spectra of the three different anti-Stokes wavelengths 515, 520, and 525 nm, we also see that the peak center moves toward lower wavenumbers, as the detection wavelength is shifted toward the blue. As expected, selecting different parts of the scattered CARS spectrum corresponds to monitoring the dynamics of different parts of the wavepacket.

An important point is the distinction between how many vibrational levels the prepared wavepacket spans on one hand versus how well the experimental technique probes these levels. Using a certain technique, we might only be able to observe coherences between a specific subset of the levels that we prepare. We are mainly limited by the Frank–
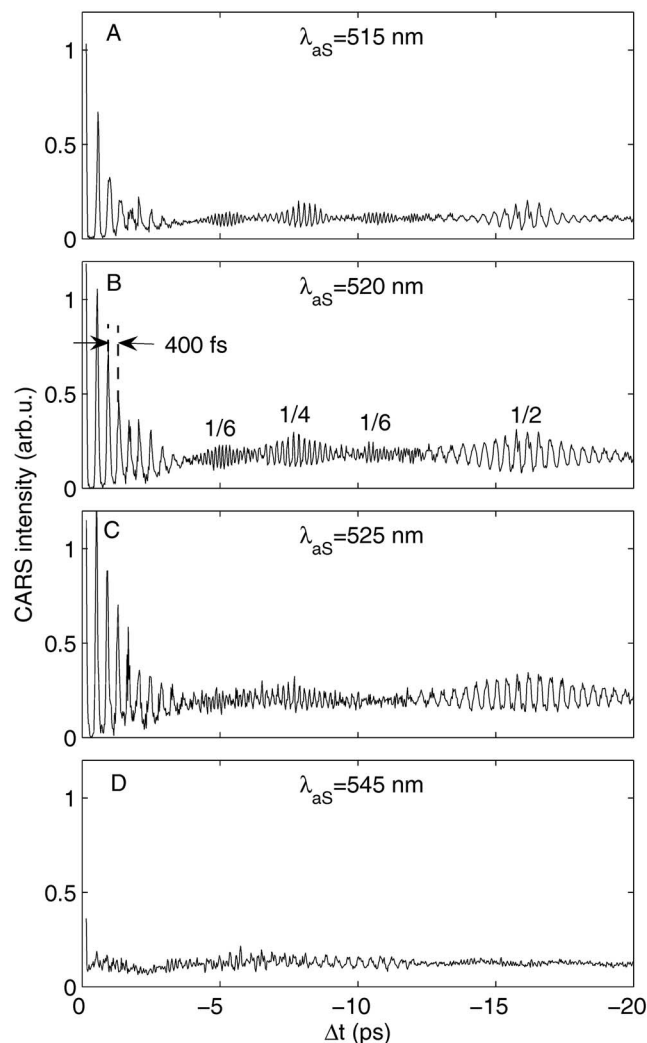
Condon factors for the probe step, which will depend on the wavelengths chosen for the experiment. In our case, where the pump and Stokes pulse spectra partially overlap, the small detuning of these wavelengths is the key to our observation of higher order revivals in the wavepacket signal, since this ensures effective probing of all the levels in the prepared state. With the time- and frequency-resolved data presented, we are thus able to follow the nuclear dynamics over a significant fraction of its periodic trajectory.

An elegant way of representing the wavepacket evolution is to use a sliding window Fourier transform or spectrogram.[38] In this method, the product of the time delay scan, $S(t)$, and a Gaussian window function, $g(t) = \exp(-t^2/t_0^2)$ and width t_0 (chosen here to be 0.75 ps) is Fourier transformed. The spectrogram signal is thus given by $S(\omega, \Delta t) = \int_0^\infty S(t) g(t - \Delta t) \exp(-i\omega t) dt$. By translating the window function along $S(t)$, we obtain a 2D map of frequency content (ω) versus time delay (Δt), with the Fourier spectral power as the intensity.[38] A plot of $\log|S(\omega, \Delta t)|^2$ for the data
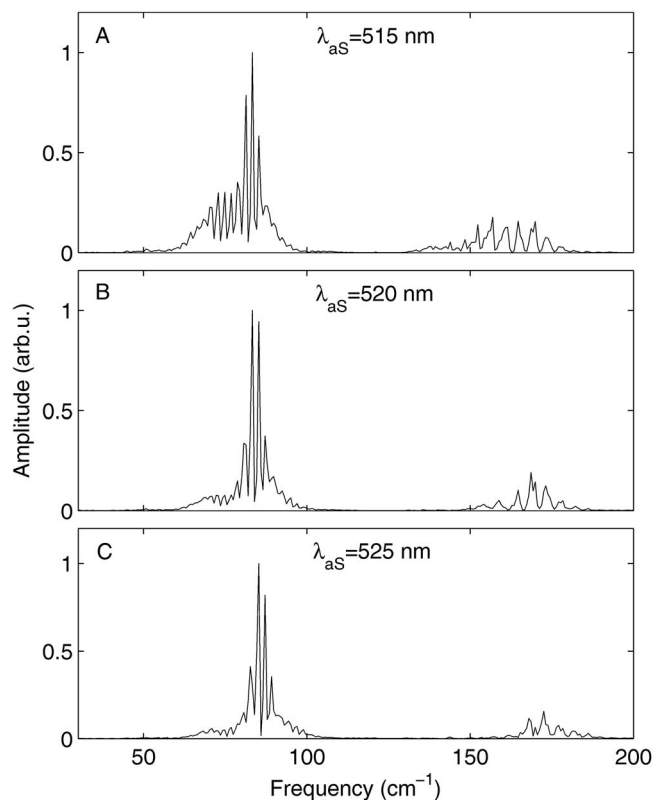
FIG. 10. Fourier transform power spectra of the iodine transients from Figs. 9(a)–9(c). As expected from wavepacket dynamics in an anharmonic potential, the peaks centered near 83 cm^{-1} correspond to the nearest-neighbor level spacings whereas as those near 170 cm^{-1} correspond to the next-nearest-neighbor level spacings. As the anti-Stokes signal wavelength moves to the blue, the level spacings in the FFT move to the red as expected (i.e., probing higher up in the excited state potential, involving more close lying vibrational levels).

FIG. 11. Log spectrogram of the CARS signal detected at 520 nm, clearly showing the time ordering of the higher frequency terms at ∼176, 250, 325, and 400 cm^{-1}. This demonstrates the high order revival structure: the second harmonics appear with twice the period of the fundamental, the third harmonic with three times, etc. This confirms the assignment of $\frac{1}{4}$, $\frac{1}{6}$, $\frac{1}{8}$, and $\frac{1}{10}$ revivals, as indicated. The $\frac{1}{10}$ revivals are the highest reported to date for a molecular wavepacket. For details see the text.

at λ_{AS}=520 nm is shown in Fig. 11. The value of the spectrogram is apparent, revealing the time ordering of the various fractional revivals of the wavepacket. The 1/4 revivals have twice the periodicity of the 1/2 revivals, the 1/6 revivals have three times the periodicity, the 1/8 revivals four times, and so on. We even observe the 1/10 revival of the B-state vibrational wavepacket in the CARS data. To our knowledge, this is the highest order fractional revival reported for a molecular wavepacket. In sum, the cuts through the 2D data of Fig. 6 at λ_{AS}=515, 520, and 525 nm reveal canonical wavepacket behavior in the iodine B-state, including wavepacket dephasing, revival, and fractional revival.

We now turn to the region of the 2D data of Fig. 6 seen on the more intense red side (530–560 nm) of the spectrum, where the intriguing "interference structures" are strongest. As an example, we show in Fig. 9(d) a cut at λ_{AS}=545 nm. This shows a significantly different behavior, with no obvious signature of wavepacket dynamics.

At the temperatures used in these experiments, several vibrational levels were initially significantly populated and, due to the use of ultrashort broad bandwidth pulses, contributions from different diagrams (as discussed in the Introduction) cannot be ruled out *a priori*. In order to investigate the consequences of these complications, we compared our experimental data with a simple analytical model wherein all relevant diagrams are considered. The basis of this model,
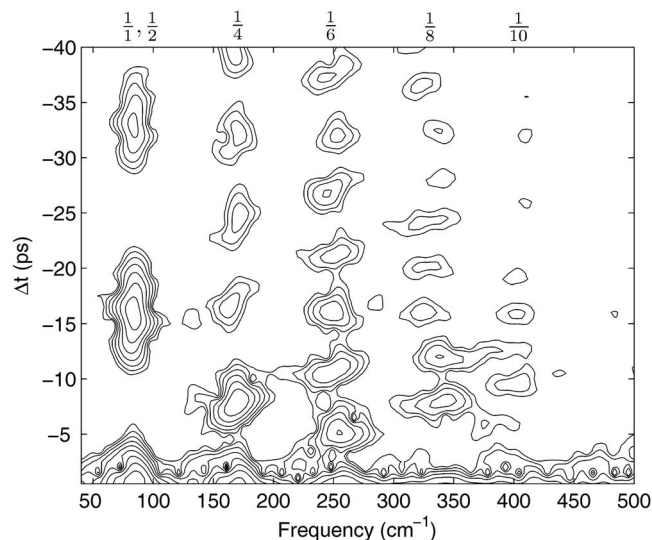
the details of which are given in the Appendix, is to restrict the electronic degree of freedom to two potential energy surfaces, with all vibrational levels within each electronic surface. The third order polarizability is calculated using perturbation theory for the density matrix. The time- and frequency-resolved CARS signal is calculated as follows:

$$S(\omega, \Delta t) = \left| \int_{-\infty}^{\infty} dt P^{(3)}(t, \Delta t) e^{i\omega t} \right|^2. \tag{4}$$

As an example, using the parameters relevant to the iodine experiment (pump ω_1=540 nm, Stokes ω_2=565 nm, transform-limited 20 fs FWHM pulses), a calculation of the contributions from both diagrams A and B of Fig. 1 at a delay time of Δt=−0.790 ps is shown in Fig. 12.

In the top panel of Fig. 12, we show the contribution from diagram A to the CARS spectrum for the various initially populated ground vibrational states. The signals from $X(v''=0)$ are in blue (full line), from $X(v''=1)$ in red (dashed line), and from $X(v''=3)$ in black (dotted line) (negligible amount). The blue and red combs are shifted with respect to each other by the X-state vibrational energy spacing ω_e, as expected. In the middle panel of Fig. 12, we show the contribution from diagram B to the CARS spectrum for the various initially populated ground vibrational states. We note that whereas diagram A emits preferentially in the high frequency part of the spectrum, diagram B emits preferentially in the low frequency part of the spectrum. Referring to the state labels (the indices of vibrational states l,k correspond to X-surface; n,m correspond to B-surface) given in Fig. 1, the major pathway for diagram A $l=1$, $n=28$, $k=4$, $m=36$ generates a signal at emission frequency $\omega_{ml}=\omega_p+\Omega$. For diagram B via $l=1$, $n=28$, $k=1$, $m=20$, the generated signal
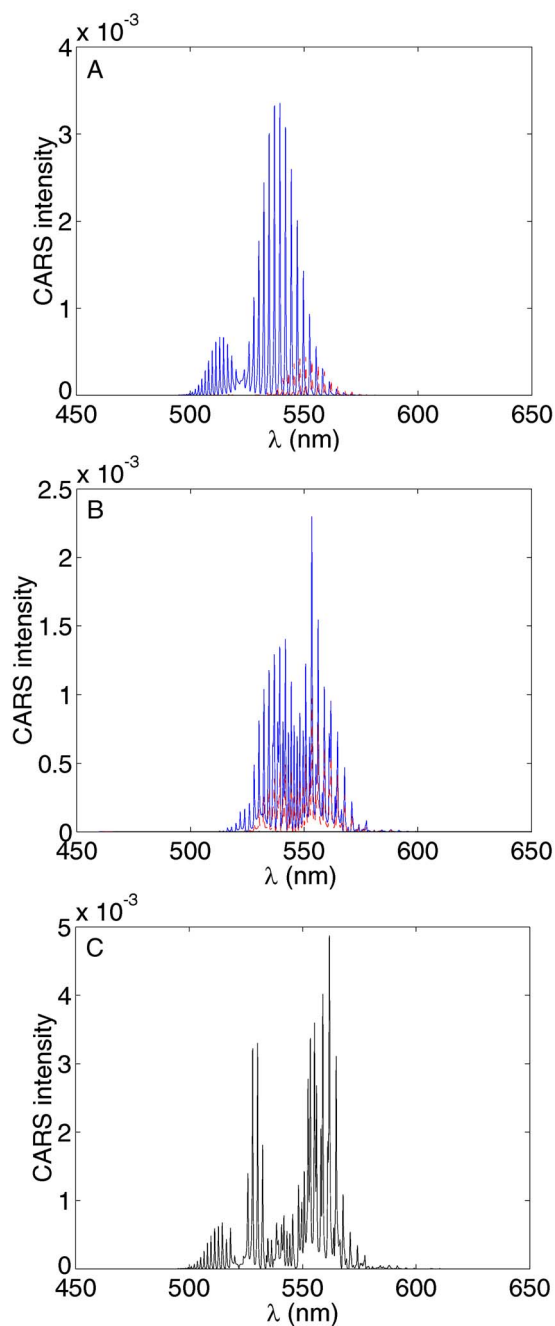
FIG. 12. (Color online) Calculated contribution of different diagrams. Delay time $\Delta t = -0.790$ ps, decoherence time 0.4 ps. The top panel shows contribution of diagram A, starting from different vibrational levels [full $v''=0$, dashed $v''=1$, and dotted $v''=2$ (very small signal)]. The central panel shows the contribution of diagram B, and shown in the bottom panel is the total spectrum. Details of the calculation of these are given in the Appendix.

emits at the pump frequency $\omega_{nk} = \omega_p$. The bottom panel shows the total signal expected from the coherent sum of the two contributing diagrams.

We note that for diagram B of Fig. 1, emission from a process starting in $v''=0$ alone contains several combs shifted by multiples of Ω due to the contribution of different k (i.e., the sample is vibrationally hot). Therefore, diagram B should yield broader spectra than diagram A. In general, diagram B does not necessarily contribute to the CARS signal for large detuning of the Stokes pulse from the electronic resonance, as discussed in the Introduction. In our case, how-

ever, we deliberately chose a sample which has initially populated vibrationally excited states in X, and a broadband Stokes pulse. Both of these aspects conspire to make diagram B significant. The complex structure within the spectra is due to the Franck–Condon factors.

Importantly, the time dynamics along a frequency cut are also different for diagrams A and B. This can be seen from Fig. 9 where panels (A)–(C) reflect predominantly the contributions from diagram A whereas panel (D) reflects that predominantly of diagram B. As opposed to diagram A, diagram B does not show any clear revival structures. The reason for this can be understood by considering Eqs. (A15) and (A16) from the Appendix. By choosing a frequency cut ω, we select a certain transition due to the resonance energy denominator. The delay-dependent phase is the same for both diagrams but the resonance energy denominators are different. Therefore, if we choose a frequency cut ω for diagram B, we strongly limit the number of n contributing to the signal [see Fig. 1 and Eq. (A16)]. For a transition starting from the ground vibrational state X ($l=1$), we predominantly go to $k=1$ which uniquely determines the n contributing to the sum. No wonder one does not see revivals—there is nothing to revive! The emission from diagram A, on the other hand, does not come from the n-levels. Therefore selecting a frequency cut does not limit the number of n-levels involved and, therefore, the coherent excitation of these levels results in the usual wavepacket revival structure. Since the two diagrams emit in different frequency regions, by making the appropriate frequency cuts as shown in Fig. 9, we are able to isolate signals due to diagram A alone.

We now consider two extremal frequency cuts, at 515 and 550 nm, using the pole approximation[39] to calculate the two-photon matrix elements (see the Appendix). As discussed above, the high frequency part of the spectrum is dominated by the signal coming from diagram A. In Fig. 13 we show contributions from the two diagrams and for all initially populated vibrational levels. For 515 nm, the signal mostly comes from diagram A for $v''=0$. The signal from diagram B shows little time structure but it does not significantly contribute to the total signal at 515 nm. Therefore, the canonical wavepacket revival structures can be observed. The situation changes dramatically for the 550 nm frequency cut shown in Fig. 14. In this case, diagram B dominates the contribution and the overall time dynamics does not show wavepacket revivals.

In our experiments, a pump wavelength of 540 nm means that at the second pump interaction, the wavepacket is projected onto the dissociative continuum of the B-state. Consequently, in calculating the third order susceptibility, one has to both sum over bound state and integrate over continuum contributions. Faeder *et al.*[10] did a thorough study of the situation when probing both above and below this threshold. These authors showed how anomalous peaks in the frequency spectrum found only when probing above the dissociation threshold could be assigned as polarization beats. The polarization generated from initial state $v''=0$ in one molecule and $v''=1$ in another gives rise to two polarizations $P_i(\omega)$ and $P_{i'}(\omega)$. In the case of probing below the threshold, these polarizations consist of narrow, nonoverlap-
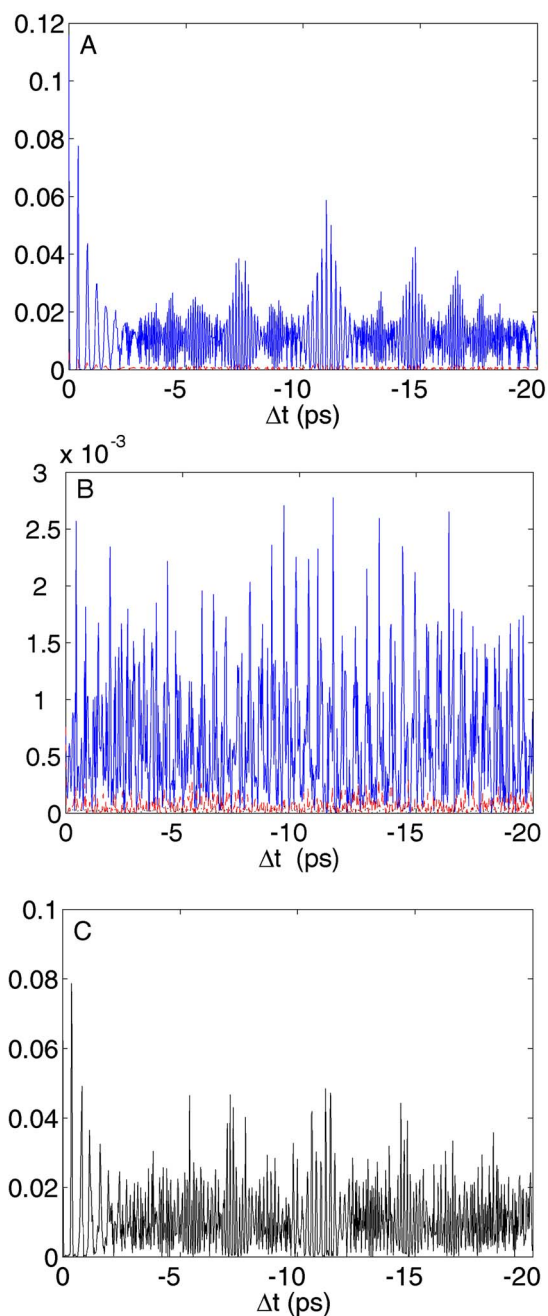
FIG. 13. (Color online) Delay time dependence of the CARS signal at the signal wavelength 515 nm. The top panel shows the CARS signal corresponding to diagram A, calculated using Eq. (A20), starting from vibrational levels $v''=0$ (full line), $v''=1$ (dashed), and $v''=2$ (dotted) (very small signal). The CARS signal corresponding to diagram B, calculated using Eq. (A22), is shown in the middle. The panel at the bottom shows the coherent sum of the two diagrams. All contributions were calculated using the pole approximation.
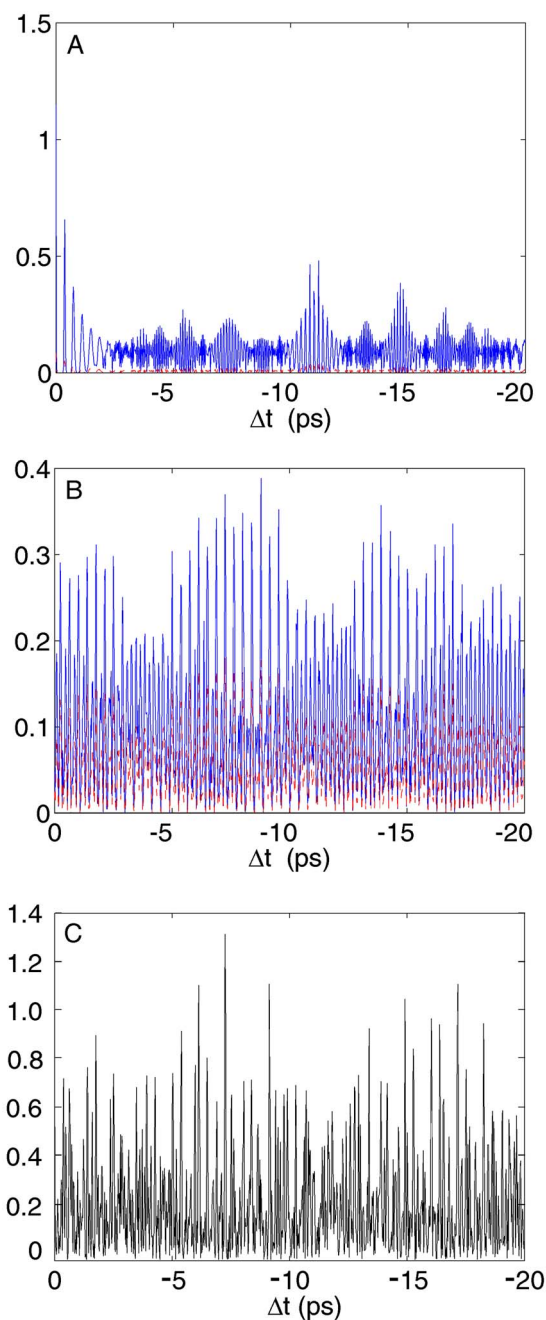
FIG. 14. (Color online) Delay time dependence of the CARS signal at the signal wavelength 550 nm. The top panel shows the CARS signal corresponding to diagram A, calculated using Eq. (A20), starting from vibrational levels $v''=0$ (full line), $v''=1$ (dashed), and $v'=2$ (dotted) (very small signal). The signal corresponding to diagram B, calculated using Eq. (A22), is shown in the middle. The panel at the bottom shows the dynamics for the coherent sum of the two diagrams. All contributions were calculated using the pole approximation.

ping lines, resulting in little interference in the resulting signal spectrum when the fields generated are squared on the detector. When probing above threshold, however, the polarizations will be short lived (i.e., spectrally broad) and overlap well, giving rise to large interferences (polarization beats). Starting from a vibrationally hot sample, the signal from a CARS experiment ending above the dissociation threshold after the second pump interaction would therefore be modulated by the splitting between $v''=0$ and $v''=1$ in the

ground state. Comparing our results with Faeder *et al.*, we see in Fig. 8 these same sidebands (marked *) on the main peak in the Fourier transform power spectra and therefore assign these peaks to this effect.

Finally, we also investigated wavepacket dynamics as probed by ultrashort pulse CARS spectroscopy in bromine and iodine bromide. An example of the CARS signal from bromine is shown in Fig. 15. As shown, we again observe vibrational wavepackets in both ground and excited states of
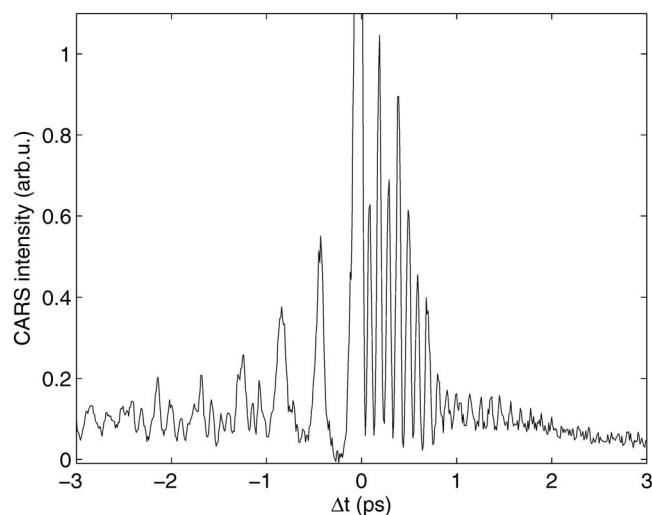
FIG. 15. A section of the CARS data for Br_2 at 543 nm, where the signal would be expected to be strongest based on the center wavelength of the pulses used. For negative (positive) delays the signal probes a vibrational wavepacket in the excited (ground) electronic state.

bromine. It should be mentioned that this result agrees very well with earlier results[40] except that these researchers did not observe ground state wavepacket dynamics due to the narrower bandwidths of their laser pulses. A typical section of the CARS data for iodine bromide is shown in Fig. 16. We again see a vibrational wavepacket in the ground electronic state at positive time delays. Interestingly, despite the exceptional signal-to-noise ratio, we see absolutely no sign of an excited state wavepacket signal. This is surprising because earlier pump-probe experiments on iodine bromide based on time-resolved photoionization[32] showed very clear excited state wavepacket dynamics in IBr, at the same wavelengths employed here. We note that, distinct from iodine and bromine, iodine bromide is predissociative in this wavelength range and undergoes interesting spin-orbit induced nonadiabatic dynamics.[32] In our opinion, this intriguing result merits
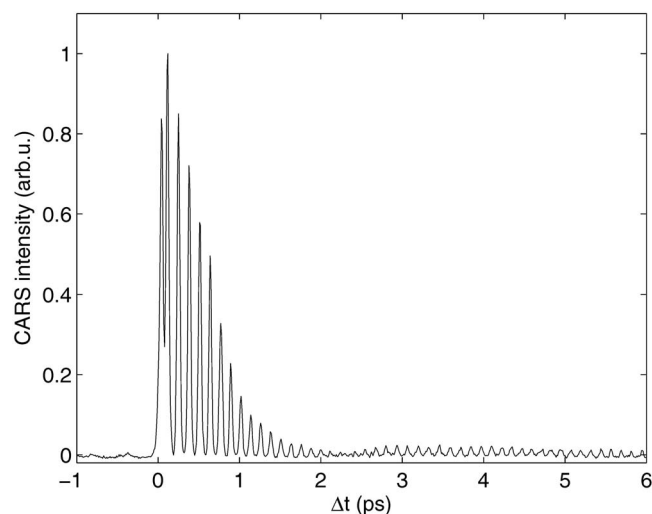

FIG. 16. A section of the CARS data for IBr at 520 nm, where the signal would be expected to be strongest, based on the center wavelength of the pulses used. For positive delays the signal probes a vibrational wavepacket in the ground electronic state. At negative delays no signal is observed. For a discussion, see the text.

more consideration as it addresses issues relating to the role of excited state electronically nonadiabatic processes in generating the CARS signals. We note that at both positive (ground state) and negative (excited state) time delays, the emitted third order polarization originates from the same set of continuum states. We speculate that the panoply of electronic states in the vicinity of the IBr *B*-state may lead to a rapid electronic dephasing of the initially created wavepacket, diminishing the excited state signal. However, this clearly requires more study.

V. CONCLUSION

Ongoing worldwide efforts in laser technology research lead to increasingly ultrashort visible light pulses. The high intensity but short duration of these pulses makes them ideal for various forms of nonlinear optical spectroscopy and these are now applied to problems such as molecular dynamics in condensed phases. We discussed the use of such ultrashort pulses for time- and frequency-resolved CARS experiments. The very broad bandwidths of these ultrashort pulses, however, introduce potential complications due to the possible spectral overlap, and therefore interference, of other third order processes contributing to the signal. These were illustrated schematically in Fig. 1. Furthermore, for complex systems and/or environments, the possibility of having a broad distribution of initial states compounds these complications. As it may be difficult to discern these various contributions in the dynamics of an uncharacterized system, it is therefore valuable to consider their effects in a simple model system.

In order to explicitly illustrate these issues in the most transparent manner, we chose gas phase molecular iodine as a model system. We employed a new achromatic dispersion-free, polarization maintaining time- and frequency-resolved CARS spectrometer together with sub-25 fs pump and Stokes laser pulses, and a heatable sample cell. We also developed a simple analytical model, based on the pole approximation, which allows one to quickly evaluate various competing contributions to the third order signal. This model allowed us to disentangle the contributions from the various diagrams and to discern the role of the different initially populated (vibrational) states in the heated sample.

This study illustrates how some care may be required when applying ultrashort pulse NLO spectroscopies such as CARS to more complex larger molecules in possibly complex environments, where the spectral and time dependence of the different third order contributions may be unknown. In order to most transparently reflect the desired molecular dynamics in the third order signals, it is important that experiments are designed such that a single diagram dominates the signal. The choices of wavelengths, bandwidths, and the timing of the three pulses involved in the process are the parameters that can be adjusted in order to achieve this selectivity.

many helpful discussions and Dr. T. Siebert (Berlin) for help in the initial phases of this experiment. We thank Doug Moffatt for technical assistance.

APPENDIX: AN ANALYTICAL MODEL

In this section we derive analytical formulas for the CARS process using standard time-dependent perturbation theory for the density matrix.[7] Atomic units (a.u.) are used throughout. Following the notation of Ref. 10, we consider the Hamiltonian of a molecule $\hat{H}_{\text{mol}}$ with two electronic states, g and e:

$$\hat{H}_{\text{mol}} = \sum_l |gl\rangle\langle gl|\omega_{gl} + \sum_n |en\rangle\langle en|\omega_{en}. \tag{A1}$$

We describe the coupling to the laser field in the rotating wave approximation:

$$\hat{V} = -\hat{\mu}^+ E(t) - \hat{\mu}^- E^*(t), \tag{A2}$$

$$\hat{\mu}^+ = \sum_{ln} |en\rangle\langle gl|\mu_{nl}, \tag{A3}$$

$$\hat{\mu}^- = \sum_{ln} |gl\rangle\langle en|\mu_{ln}. \tag{A4}$$

Here n, l indicate the adiabatic rovibrational eigenstates, and $\mu_{nl} = \langle en|\hat{\mu}|gl\rangle$. The laser field $E(t)$ in Eq. (A2) is specified as follows:

$$E = E_1(t) + E_2(t) + E_3(t), \tag{A5}$$

$$E_i(t) = E_0 e^{-(t-t_i)^2/2\sigma^2} e^{-i\omega_i(t-t_i)+i\mathbf{k}_i\mathbf{r}}, \tag{A6}$$

where $i=1$ describes the first pump pulse, $i=2$ describes the Stokes pulse, <u>and</u> $i=3$ describes the second pump pulse, $\sigma = \text{FWHM}_t/2\sqrt{\ln 2}$, and FWHM_t is the full width at half maximum of the pulse intensity.

The perturbation theory for the density operator yields

$$i\dot{\rho}'^{(q)} = [\hat{V}', \rho'^{(q-1)}]. \tag{A7}$$

Here the density operator $\rho'(t)$ and the operator for the interaction with the laser field are written in the interaction representation:

$$\hat{\rho}'(t) = e^{i\hat{H}_{\text{mol}}t}\hat{\rho}e^{-i\hat{H}_{\text{mol}}t}, \tag{A8}$$

$$\hat{V}'(t) = e^{i\hat{H}_{\text{mol}}t}\hat{V}e^{-i\hat{H}_{\text{mol}}t}. \tag{A9}$$

Within this approach the induced dipole moment describing the qth order polarization can be written as

$$\langle d_\alpha(t)\rangle^{(q)} = i^q \int dt_1 \cdots \int dt_q \theta(t-t_1)\cdots\theta(t-t_q)$$
$$\times \text{Sp}\{\rho[\cdots[V'(t), V'(t_1)], \ldots, V'(t_q)]\}, \tag{A10}$$

where ρ is the unperturbed density operator. The function $\theta(t)$

$$\theta(t) = e^{-\gamma t} \quad (t > 0) \tag{A11}$$

$$\theta(t) = 0 \quad (t < 0) \tag{A12}$$

is introduced to take into account the casuality and inevitable damping γ due to the reasons discussed above.

The CARS process is driven by the third order polarization induced in the medium $P^{(3)} = N\langle d\rangle^{(3)}$, where N is the density of molecules in the medium. For $\langle d\rangle^{(3)}$ the triple commutator in Eq. (A10) gives rise to eight terms corresponding to eight diagrams described in detail in Ref. 10 (see Fig. 3 of Ref. 10). In our case, when the pump pulse does not overlap with the Stokes/pump pulse pair, only diagrams A–E shown in Fig. 1 survive. In the following we show the corresponding contributions of the induced dipoles obtained using Eq. (A10) with $q=3$. We will not consider rotational degrees of freedom and, for convenience, omit the electronic indices g, e for the frequencies and matrix elements. Therefore, it is useful to keep in mind that l, k numerate vibrational states on the X-surface and m, n numerate vibrational states on the B-surface.

The negative delay times, when the first pump pulse arrives before the Stokes/pump pulse pair (excited state CARS), correspond to diagram A. Consequently, one obtains for $d^{\text{A}}(t, \tau)$:

$$d^{\text{A}}(t, \tau) = 2\pi i \sum_{l,m,n,k} \rho_{ll} e^{-i\omega_{nl}\tau} e^{i\omega_{ln}t} \mu(l,m,n,k)\mathcal{E}_1(\omega_{nl}) \times \int d\omega' d\omega'' \frac{\mathcal{E}_2(\omega')\mathcal{E}_3(\omega'')e^{i(\omega'-\omega'')t}}{(\omega' + \omega_{kn} - i\gamma)(\omega' + \omega_{mn} - \omega'' - i\gamma)} + \text{c.c.} \tag{A13}$$

Here τ is a delay time between the arrival of the pump pulse and Stokes/pump pulse pair, $(\tau = -\Delta t)$, $\omega_{ij} = \omega_i - \omega_j$ and $\mu(l,m,n,k) \equiv \mu_{lm}\mu_{nl}\mu_{kn}\mu_{mk}$. The sum over l accounts for the fact that several vibrational states in the ground electronic surface can be initially incoherently populated. The corresponding weight of these states is given by the diagonal elements of the equilibrium density matrix determined from

the Boltzmann distribution (see below).

$\mathcal{E}_1(\omega)$, $\mathcal{E}_2(\omega)$, and $\mathcal{E}_3(\omega)$ represent the Fourier transforms of the laser pulses specified in Eq. (A6). In deriving Eq. (A13), we assumed that the pump pulse does not overlap with the Stokes/pump pulse pair and extended the upper limit of the corresponding time integral to infinity. This explains the appearance of the pump pulse Fourier components

$\mathcal{E}_1(\omega_{nl})$ at the frequencies of the corresponding transitions ω_{nl}. The emission spectrum is calculated by performing the Fourier transform over t:

$$d^{\mathrm{A}}(\omega,\tau) = \frac{1}{2\pi}\int dt\, d^{\mathrm{A}}(t,\tau)e^{i\omega t} \tag{A14}$$

and yields

$$d^{\mathrm{A}}(\omega,\tau) = 2\pi i \sum_{l,m,n,k} \rho_{ll} e^{-i\omega_{nl}\tau}\mu(l,m,n,k)\mathcal{E}_1(\omega_{nl})$$
$$\times \int d\omega'\frac{\mathcal{E}_2(\omega')\mathcal{E}_3(\omega_{ln}+\omega'+\omega)}{(\omega'+\omega_{kn}-i\gamma)(\omega_{ml}-\omega-i\gamma)} + \mathrm{c.c.} \tag{A15}$$

The integral over ω' in Eq. (A15) describes both resonant and nonresonant populations of the intermediate level k, leading to the real populations in m. The phenomenological damping factor γ reflects phase decoherence (transverse relaxation). The relaxation of population (longitudinal relaxation) is negligible and is not considered here.

Analogously, one obtains for $d^{\mathrm{B}}(\omega,\tau)$, corresponding to the diagram B:

$$d^{\mathrm{B}}(\omega,\tau) = -2\pi i \sum_{l,m,n,k} \rho_{ll} e^{-i\omega_{nl}\tau}\mu(l,m,n,k)\mathcal{E}_1(\omega_{nl})$$
$$\times \int d\omega'\frac{\mathcal{E}_2(\omega')\mathcal{E}_3(\omega'+\omega-\omega_{nl})}{(\omega_{ml}-\omega'+i\gamma)(\omega+\omega_{kn}+i\gamma)} + \mathrm{c.c.} \tag{A16}$$

This expression is valid for both positive and negative delay times: diagrams B and E yield equivalent results, $d^{\mathrm{B}}(\omega,\tau)=d^{\mathrm{E}}(\omega,-\tau)$. However, this does not mean that the resulting dynamics will be the same: the phase factors for $d^{(\mathrm{B})}$ and $d^{(\mathrm{E})}$ have opposite signs.

For positive delay times (ground state CARS), when the pump/Stokes pulse pair arrives before the second pump pulse, the dipole moment corresponding to diagram C, $d^{\mathrm{C}}(\omega,\tau)$, $(\tau=+\Delta t)$, is given by

$$d^{\mathrm{C}}(\omega,\tau) = 2\pi i \sum_{l,m,n,k} \rho_{ll} e^{i(\omega_{lk}+\omega)\tau}\mu(l,m,n,k)\mathcal{E}_3(\omega_{lk}+\omega)$$
$$\times \int d\omega'\frac{\mathcal{E}_2(\omega_{lk}+\omega')\mathcal{E}_1(\omega')}{(\omega'-\omega_{nl}+i\gamma)(\omega_{ml}-\omega-i\gamma)} + \mathrm{c.c.} \tag{A17}$$

In a similar fashion, the dipole moment, $d^{\mathrm{D}}(\omega,\tau)$, corresponding to diagram D, can be found:

$$d^{\mathrm{D}}(\omega,\tau) = -4\pi^2 i \sum_{l,m,n,k} \rho_{kk}\mu(k,l,m,n)$$
$$\times \frac{\mathcal{E}_1(\omega_{mk})\mathcal{E}_2(\omega_{nk})\mathcal{E}_3(\omega_{nm}+\omega)}{(\omega+\omega_{lm}+i\gamma)}e^{i(\omega_{nm}+\omega)\tau} + \mathrm{c.c.} \tag{A18}$$

In deriving Eq. (A18), we assumed that the pump/Stokes pulse pair does not overlap with the delayed pump pulse and extended the upper limit of the corresponding time integral to infinity. This explains the appearance of the pump and

Stokes pulse Fourier components $\mathcal{E}_1(\omega_{mk})$ and $\mathcal{E}_2(\omega_{nk})$ at the frequencies ω_{mk} and ω_{nk} of the corresponding transitions. This diagram probes excited state dynamics.

To calculate transition frequencies and matrix elements in Eqs. (A15), (A17), and (A16), we used electronic potential surfaces from Ref. 21 and transition dipole moments from Ref. 41. We consider a 540 nm ($\omega_1=0.0843$ a.u.) pump pulse and 565 nm ($\omega_2=0.0806$ a.u.) Stokes pulse. The pump pulse excites the $B\leftarrow X$ transition page in iodine: $B(28)-X(0)$ $=0.0848$ a.u.. The detuning between the pulses (Ω $=0.0037$ a.u.) corresponds to the energy difference between $X(4)=0.004$ a.u. and $X(0)=0.0005$ a.u. levels in iodine. For the analytical calculations, we used the Fourier images of the pulse envelopes in frequency domain:

$$\mathcal{E}_i(\omega) = F[E_i(t)] = \sqrt{2\pi}\sigma E_0 e^{-(\omega-\omega_i)^2\sigma^2/2}. \tag{A19}$$

For $\mathrm{FWHM}_t=20$ fs, $\mathrm{FWHM}_w=0.0034$ a.u. and therefore the pump pulse can excite nine vibrational states within the FWHM_ω of the pulse bandwidth: $B(33)-B(24)=0.0034$ a.u. The same bandwidth was chosen for the Stokes pulse. In our calculations, we included 40 vibrational levels in the X-state and 54 vibrational levels in the B-state. For the temperature chosen in the experiment (360 K corresponding to 0.001 a.u.), three vibrational states in the X-state were initially populated according to the Boltzmann distribution ρ_{ll} $=e^{-\beta E_l}$, $\beta=1000$ a.u.. We set the phase relaxation width to $\gamma=3\times 10^{-5}$ a.u., which corresponds to a decoherence time of $1/(2\gamma)=0.4$ ps and partially includes the experimental signal decay due to the rotational anisotropy.

To speed up the calculation of the two-photon transition matrix elements, we used the pole approximation[39] leading to the following expression for diagram A:

$$d_r^{\mathrm{A}}(\omega,\tau) = -2\pi^2 \sum_{l,m,n,k} \rho_{ll} e^{-i\omega_{nl}\tau}\mu(l,m,n,k)\mathcal{E}_1(\omega_{nl})$$
$$\times \frac{\mathcal{E}_2(\omega_{nk})\mathcal{E}_3(\omega_{lk}+\omega)}{(\omega_{ml}-\omega-i\gamma)} + \mathrm{c.c.} \tag{A20}$$

for diagram C:

$$d_r^{\mathrm{C}}(\omega,\tau) = 2\pi^2 \sum_{l,m,n,k} \rho_{ll} e^{i(\omega_{lk}+\omega)\tau}\mu(l,m,n,k)$$
$$\times \mathcal{E}_3(\omega_{lk}+\omega)\frac{\mathcal{E}_2(\omega_{nk})\mathcal{E}_1(\omega_{nl})}{(\omega_{ml}-\omega-i\gamma)} + \mathrm{c.c.} \tag{A21}$$

and diagram B (the same is valid for diagram E, since $d^{\mathrm{B}}(\omega,\tau)=d^{\mathrm{E}}(\omega,-\tau)$):

$$d_r^{\mathrm{B}}(\omega,\tau) = -2\pi^2 \sum_{l,m,n,k} \rho_{ll} e^{-i\omega_{nl}\tau}\mu(l,m,n,k)\mathcal{E}_1(\omega_{nl})$$
$$\times \frac{\mathcal{E}_2(\omega_{ml})\mathcal{E}_3(\omega_{mn}+\omega)}{(\omega+\omega_{kn}+i\gamma)} + \mathrm{c.c.} \tag{A22}$$

The plots of signal spectrum at a specific time delay for the two contributing diagrams, shown in Fig. 12, and the plots of signal strength at a specific wavelength as a function of delay time, shown in Fig. 13 and Fig. 14 were based on Eq. (A20) for signals diagram A and on Eq. (A22) for the signals from diagram B.

[1] R. Ell, U. Morgner, F. X. Kärtner, J. G. Fujimoto, E. P. Ippen, V. Scheuer, G. Angelow, T. Tschudi, M. J. Lederer, and A. Boiko, and B. Luther-Davies, Opt. Lett. **26**, 373 (2001).

[2] I. Jung, F. X. Kärtner, N. Matuschek, D. Sutter, F. Morier-Genoud, Z. Shi, V. Scheuer, M. Tilsch, T. Tschudi, and U. Keller, Appl. Phys. B: Lasers Opt. **65**, 137 (1997).

[3] T. Driscoll, G. Gale, and F. Hache, Opt. Commun. **110**, 638 (1994).

[4] E. Riedle, M. Beutter, S. Lochbrunner, J. Piel, S. Schenkl, S. Spörlein, and W. Zinth, Appl. Phys. B: Lasers Opt. **71**, 457 (2000).

[5] T. Kobayashi and A. Shirakawa, Appl. Phys. B: Lasers Opt. **70**, S239-S246 (2000).

[6] P. Baum, S. Lochbrunner, and E. Riedle, Appl. Phys. B: Lasers Opt. **79**, 1027 (2004).

[7] S. Mukamel, *Principles of Nonlinear Optical Spectroscopy* (Oxford University Press, Oxford, 1995).

[8] V. V. Lozovoy, B. I. Grimberg, E. J. Brown, I. Pastirkz, and M. Dantus, J. Raman Spectrosc. **31**, 41 (2000).

[9] T. Siebert, M. Schmitt, A. Vierheilig, G. Flachenecker, V. Engel, A. Materny, and W. Kiefer, J. Raman Spectrosc. **31**, 25 (2000).

[10] J. Faeder, I. Pinkas, G. Knopp, Y. Prior, and D. J. Tannor, J. Chem. Phys. **115**, 8440 (2001).

[11] T. Chen, V. Engel, M. Heid, W. Kiefer, G. Knopp, A. Materny, S. Meyer, R. Pausch, M. Schmitt, and H. Schwoerer, and T. Siebert, J. Mol. Struct. **480–481**, 33 (1999).

[12] R. M. Bowman, M. Dantus, and A. H. Zewail, Chem. Phys. Lett. **161**, 297 (1989).

[13] M. Gruebele and A. H. Zewail, J. Chem. Phys. **98**, 883 (1993).

[14] I. Fischer, D. M. Villeneuve, M. J. J. Vrakking, and A. Stolow, J. Chem. Phys. **102**, 5566 (1995).

[15] H. Stapelfeldt, E. Constant, and P. Corkum, Phys. Rev. Lett. **74**, 3780 (1995).

[16] M. Schmitt, G. Knopp, A. Materny, and W. Kiefer, Chem. Phys. Lett. **270**, 9 (1997).

[17] M. Gutmann, D. M. Willberg, and A. H. Zewail, J. Chem. Phys. **97**, 8037 (1992).

[18] M. Karavitis, D. Segale, Z. Bihary, M. Pettersson, and V. A. Apkarian, Low Temp. Phys. **29**, 814 (2003).

[19] G. Flachenecker, P. Behrens, G. Knopp, M. Schmitt, T. Siebert, A. Vierheilig, G. Wirnsberger, and A. Materny, J. Phys. Chem. A **103**, 3854 (1999).

[20] G. Knopp, I. Pinkas, and Y. Prior, J. Raman Spectrosc. **31**, 51 (2000).

[21] S. Gerstenkorn and P. Luc, *Atlas du Spectre d'Absorption de la Molecule d'Iode* (CNRS II, Paris, 1978).

[22] J. H. Eberly, N. Narozhny, and J. J. Sanchez-Mondragon, Phys. Rev. Lett. **44**, 1323 (1980).

[23] I. S. Averbukh and N. Perelman, Phys. Lett. A **139**, 449 (1989).

[24] O. Knospe and R. Schmidt, Phys. Rev. A **54**, 1154 (1996).

[25] C. Leichtle, I. S. Averbukh, and W. P. Schleich, Phys. Rev. Lett. **77**, 3999 (1996).

[26] V. A. Ermoshin, M. Erdmann, and V. Engel, Chem. Phys. Lett. **356**, 29 (2002).

[27] T. Lohmüller, V. Engel, J. A. Beswick, and C. Meier, J. Chem. Phys. **120**, 10442 (2004).

[28] H. Katsuki, H. Chiba, B. Girard, C. Meier, and K. Ohmori, Science **311**, 1589 (2006).

[29] A. Stolow, M. J. J. Vrakking, and D. M. Villeneuve, Phys. Rev. A **54**, R37 (1996).

[30] I. S. Averbukh, A. Stolow, M. J. J. Vrakking, and D. M. Villeneuve, Phys. Rev. Lett. **77**, 3518 (1996).

[31] M. J. J. Vrakking, D. M. Villeneuve, and A. Stolow, J. Chem. Phys. **105**, 5647 (1996).

[32] M. Shapiro, M. J. J. Vrakking, and A. Stolow, J. Chem. Phys. **110**, 2465 (1999).

[33] S. Meyer, M. Schmitt, A. Materny, W. Kiefer, and V. Engel, Chem. Phys. Lett. **301**, 248254 (1999).

[34] S. Meyer, M. Schmitt, A. Materny, W. Kiefer, and V. Engel, Chem. Phys. Lett. **281**, 332 (1997).

[35] M. Schmitt, G. Knopp, A. Materny, and W. Kiefer, Chem. Phys. Lett. **280**, 339 (1997).

[36] T. Siebert, M. Schmitt, T. Michelis, A. Materny, and W. Kiefer, J. Raman Spectrosc. **30**, 807 (1999).

[37] R. Maksimenka, B. Dietzek, A. Szeghalmi, T. Siebert, W. Kiefer, and M. Schmitt, Chem. Phys. Lett. **408**, 3743 (2005).

[38] I. Fisher, M. J. J. Vrakking, D. M. Villeneuve, and A. Stolow, Chem. Phys. **207**, 331 (1996).

[39] M. V. Fedorov, *Interaction of Intense Laser Light With Free Electrons* (Routledge, London, 1991).

[40] M. Schmitt, G. Knopp, A. Materny, and W. Kiefer, J. Phys. Chem. A **102**, 4059 (1998).

[41] J. Tellinghuisen, J. Chem. Phys. **106**, 1305 (1997).